Mechanism of Ferric Oxalate Photolysis

David. M. Mangiante[†], Richard D. Schaller[‡], Piotr Zarzycki[†§], Jillian F. Banfield[†∥], and Benjamin Gilbert[*†]

[†] Energy Geosciences Division, Lawrence Berkeley National Laboratory, 1 Cyclotron Road, Berkeley, California 94720, United States

[‡] Center for Nanoscale Materials, Argonne National Laboratory, 9700 South Cass Avenue, Building 440, Argonne, Illinois 60439, United States

[§] Institute of Physical Chemistry, Polish Academy of Sciences, 01-224 Warsaw, Poland

[∥] Department of Earth and Planetary Science, University of California, Berkeley, Berkeley, California 94720, United States

ACS Earth Space Chem., **2017**, *1* (5), pp 270–276

DOI: 10.1021/acsearthspacechem.7b00026

Publication Date (Web): June 8, 2017

*E-mail: bgilbert@lbl.gov.

Abstract

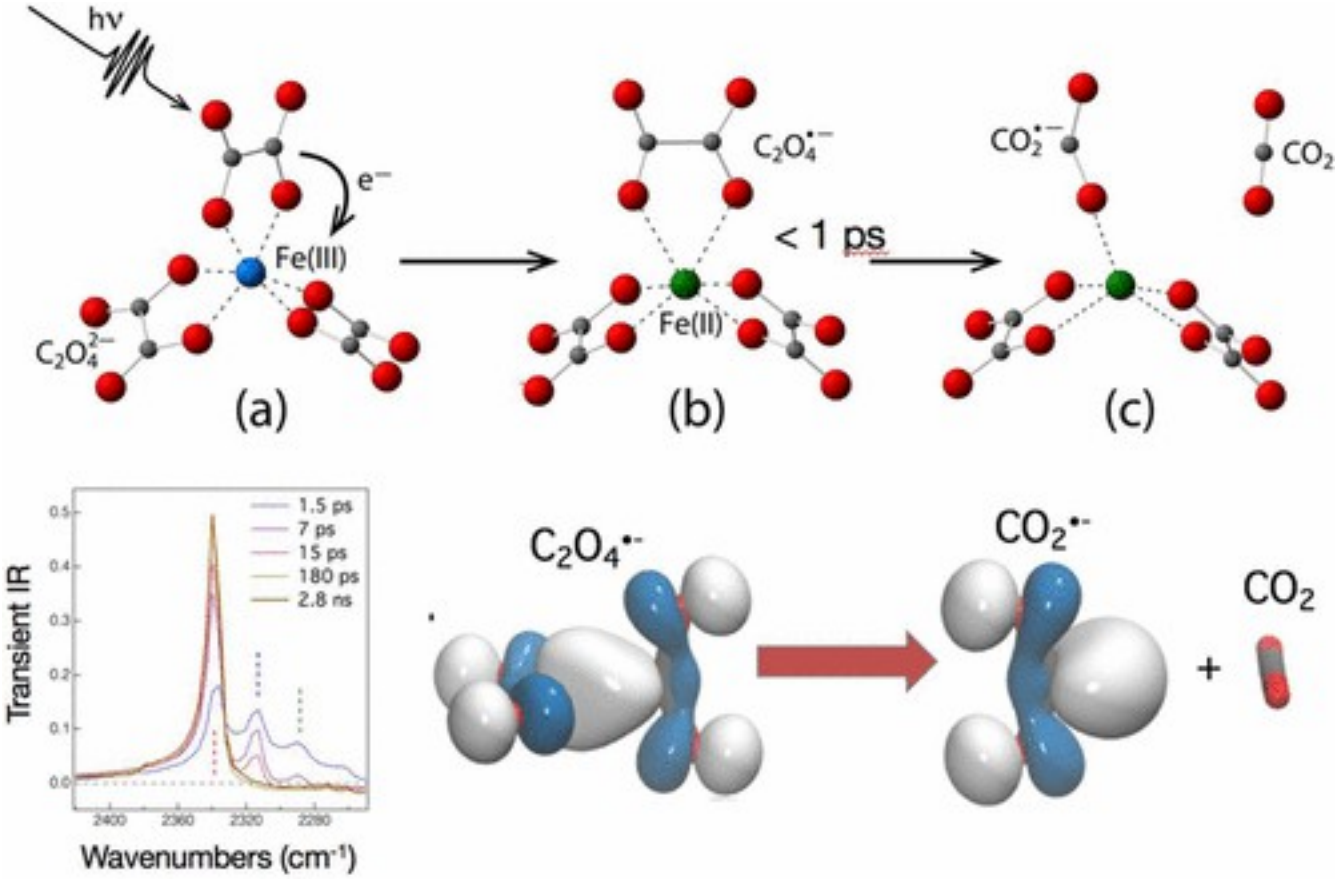

Iron(III) oxalate, $Fe^{3+}(C_2O_4)_3^{3-}$, is a photoactive metal organic complex found in natural systems and used to quantify photon flux as a result of its high absorbance and reaction quantum yield. It also

serves as a model complex to understand metal carboxylate complex photolysis because the mechanism of photolysis and eventual production of CO_2 is not well understood for any system. We employed pump/probe mid-infrared transient absorption spectroscopy to study the photolysis reaction of the iron(III) oxalate ion in D_2O and H_2O up to 3 ns following photoexcitation. We find that intramolecular electron transfer from oxalate to iron occurs on a sub-picosecond time scale, creating iron(II) complexed by one oxidized and two spectator oxalate ligands. Within 40 ps following electron transfer, the oxidized oxalate molecule dissociates to form free solvated $CO_{2(aq)}$ and a species inferred to be $CO_2^{\cdot -}$ based on the appearance of a new vibrational absorption band and *ab initio* simulation. This work provides direct spectroscopic evidence for the first mechanistic steps in the photolysis reaction and presents a technique to analyze other environmentally relevant metal carboxylate photolysis reactions.

Keywords:
carbon dioxide radical anion; metal cycling; mid-infrared vibrational spectroscopy; photochemistry; ultrafast spectroscopy

1 Introduction

Dissolved iron in natural waters is commonly complexed by small organic molecules through carboxylic acid functional groups.(1) Fe(III) carboxylate complexes are typically more photoactive than either of the unbound species because complexation introduces new optical absorption bands associated with electron transfer from the organic to unoccupied states of the metal.(2)Ligand-to-metal charge-transfer (LMCT) transitions can cause iron reduction and initiate the oxidative degradation of organic acids.(3) These photolysis reactions are important in the iron redox cycle and major pathways for the mineralization of dissolved organic matter (DOM) in sunlit waters and atmospheric aerosol particles.(4-7) Moreover, they can be harnessed for organic contaminant degradation.(8, 9)

Numerous organic acids, including tartrate, lactate, malonate, and pyruvate, undergo similar complexation and photolysis reactions with iron.(1, 10) Oxalate is an important dicarboxylic acid that is produced by plants, fungi, and some bacteria. It forms a strong complex with iron(III) to form ferrioxalate, $Fe^{III}(C_2O_4)_3^{3-}$. Ferrioxalate is also important in environmental science, where it is used to quantify the flux of light in aqueous systems.(11) We chose it as a model system for studying the mechanisms of iron carboxylate photolysis reactions.

The overall reaction upon illumination can be expressed as(12)

$$2Fe^{III}(C_2O_4)_3^{3-} \xrightarrow{h\nu} 2Fe^{II}(C_2O_4)_2^{2-} + 2CO_2 + C_2O_4^{2-} \quad (1)$$

It is generally accepted that a single photoabsorption event reduces iron and creates a radical species capable of reducing a further ferrioxalate molecule. The radical anions of both carbon dioxide, $CO_2^{\cdot -}$, and oxalate, $C_2O_4^{\cdot -}$, have been proposed as the key reactive intermediate, but neither the identity of the intermediate nor the reaction pathway have been confidently established. Recently, several groups have studied ferrioxalate photolysis using time-resolved optical and X-ray spectroscopic methods. Chen et al. used benchtop extended X-ray absorption fine structure (EXAFS) spectroscopy at the Fe K edge with 2 ps temporal resolution to monitor Fe–O bond length changes following photoexcitation.(13) They concluded that an excited-state oxalate ion is lost from the complex. Subsequently, this decomposes to form one $CO_2^{\cdot -}$ species that reduces a second iron complex. Pozdnyakov et al. used transient optical absorption spectroscopy with 5 ns resolution and a spectral range of 310–750 nm to study microsecond optical transients in ferrioxalate solutions with and without methyl viologen, which is used to quench radicals.(14) They proposed that electron transfer from oxalate to iron forms an oxalate radical that initially remains bound to the metal and subsequently diffuses into solution. Ogi et al. used near-edge X-ray absorption fine structure (NEXAFS) at the Fe K edge with 0.2 ps resolution and observed a prompt shift of the Fe absorption threshold to lower energy, consistent with rapid iron reduction.(15) On the basis of this observation and density functional theory calculations, they proposed that electron transfer from oxalate to iron produces a bound excited molecule that dissociates as $CO_2^{\cdot -}$ and CO_2.

None of the time-resolved spectroscopic methods used to date in this system is directly sensitive to the chemical state of the organic ligand. An alternative method, infrared (IR) spectroscopy, probes the vibrational modes of molecules and complexes and is highly sensitive to specific molecules, functional groups, and bonding types. Time-resolved IR spectroscopy has been used to reveal the intramolecular electron transfer pathways as well as excited-state molecular reorganization.(16) We employed optical-pump, mid-IR probe spectroscopy with 0.1 ps resolution to detect changes in the ferrioxalate complex following optical excitation and to seek direct evidence for the formation of intermediate species. Interpretation of the vibrational spectra and complementary investigations into the fate of the products of the reaction were performed using *ab initio* and molecular dynamics simulations.

2 Experimental Section

2.1 Ferric Oxalate Synthesis

Iron(III) oxalate hexahydrate, a solid powder with a Fe/oxalate ratio of 1:1.5, was purchased from Alfar Aesar. We added anhydrous sodium oxalate powder (Sigma-Aldrich) to attain the stoichiometry of ferrioxalate and added water or deuterium oxide for a target concentration of 0.1 M. After 24 h in the dark, non-dissolved solids were separated by centrifugation and the Fourier transform infrared (FTIR) spectrum of the supernatant was measured in transmission in a 100 μm path length CaF_2 flow cell using a benchtop FTIR spectrometer (Nicolet). The samples were diluted with water or D_2O until the optical density (OD) at 1700 cm^{-1} was approximately unity. The estimated ferrioxalate concentrations were 10 mM.

2.2 Pump–Probe IR Transient Absorption Spectroscopy

We performed transient absorption (TA) spectroscopy with a 266 nm pump and mid-IR array detector at the Argonne Center for Nanoscale Materials (CNM) using an amplified femtosecond Ti/sapphire laser system at 2 kHz repetition rate. To generate the mid-IR probe, half of the laser output is directed into an optical parametric amplifier (OPA) using difference frequency generation. The remaining 800 nm power pumps a second OPA to produce the excitation pulses. The pump is variably time-delayed relative to the pump via a mechanical delay line (limited to a maximum delay of 3 ns), and a mechanical chopper blocked every other pump pulse. Probe light was directed to a 0.3 m grating spectrograph, dispersed, and detected on a 128 element gated mercury cadmium telluride array detector. Full probe spectra were acquired for each laser shot, and changes in absorbance were calculated for conditions of pump on minus pump off. The overall time resolution was 100 fs, as inferred from the cross-phase modulation during temporal overlap of the pump and probe pulses as described in ref 17. IR laser pulses were entirely housed in a sealed box purged with nitrogen to limit absorption by water vapor and other atmospheric absorbers.

Typical samples consisted of approximately 10 mM ferrioxalate dissolved in either H_2O or D_2O that was continuously sparged with nitrogen gas and pumped through a CaF_2 flow cell with a path length of ∼10 μm. These two solvents provide different absorption windows in the mid-IR, in which vibrational signatures of ferrioxalate and photolysis products could be observed. Data analysis was performed using routines written in the IgorPro software to subtract the detector background (an average of data collected at least 2 ps before time zero) and extract transient spectra and kinetic traces. The kinetic traces were fitted by exponential decay functions at a single wavenumber or by a kinetic model described below.

2.3 Molecular Simulations

We performed *ab initio* calculations using the Gaussian 09 package(18) to find the energy-minimized structure and principal IR-active vibrational modes of the oxalate ion, carbon dioxide, and candidate intermediate species. We compared density functional theory (DFT)(19) and second-order Møller–Plesset perturbation theory (MP2),(20) concluding MP2 to be more accurate. Only MP2 offered a systematic improvement toward the experimental data for the CO_2 molecule with increasing basis-set completeness (see geometric parameters and vibration frequencies in Tables S1 and S2 of the Supporting Information). In addition, the DFT frequencies depended strongly upon the exchange-correlation functional used, system size, and chosen basis set.(21)Calculations at the MP2 level with the aug-cc-pvtz basis set gave good agreement to the experimental C–O bond length and principal vibrational frequencies for CO_2.

We used molecular dynamics simulations to explore the loss of photolysis products from the coordination sphere of iron(II). The force field parameters were derived from our *ab initio*calculations in combination with the general AMBER force field (GAFF) force field.(22) The $Fe^{2+/3+}$interaction potentials are taken from the study by Li et al.(23, 24) We simulated D_2O using the extended simple point charge (SPC/E) model of water(25) with the deuterium mass (see the Supporting Information for details). The molecular dynamics was carried out using the pmemd engine from AMBER 16(26) on 32 central processing units (CPU) (Intel Xeon 3.6 GHz) and 4 graphics processing units (GPU) (NVIDIA Tesla) cluster.

3 Results and Discussion

3.1 Mid-IR Transient Absorption Spectroscopy in D_2O

Photoexcitation of ferrioxalate with 266 nm ultraviolet (UV) light in D_2O causes prompt changes in the IR spectrum in the 1600–1725 cm^{-1} range (Figure 1). We observed the loss of intensity at around 1675 cm^{-1}, the location of C–O asymmetric stretches, ν_{as}(C–O), in ferrioxalate(27) and the emergence of a new signal at around 1630 cm^{-1}, the location of the ν_{as}(C–O) band in ferrous oxalate, $Fe^{II}(C_2O_4)_2^{2-}$. We simulated transient spectra by subtracting ground-state IR data of ferrioxalate from ferrous oxalate, obtaining good agreement with the lineshapes of the transient spectra acquired within 0–2 ps (Figure 2). Photoexcitation of ferrioxalate thus rapidly generates a species with the vibrational response of ferrous oxalate. The ferrioxalate absorption at around 1660–1600 cm^{-1} appears with a rise time that is within the temporal response of the instrument (~0.1 ps), indicating that spectator oxalate ligands rapidly relax following iron reduction.

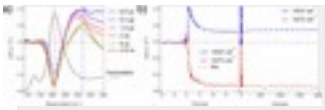

Figure 1. Transient mid-IR data for ferrioxalate in D_2O. (a) Selected transient spectra from 0 ps to 2.8 ns following photoexcitation at 288 nm. The ground-state IR spectrum for ferrioxalate dissolved in D_2O is shown in black (right axis). (b) Kinetic traces extracted at 1632 cm^{-1} (blue) and 1675 cm^{-1} (red) shown at short- and long-time scales. Kinetic fits are shown as dashed black lines in the left panel.

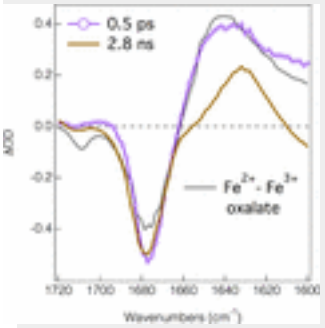

Figure 2. Transient mid-IR spectra for ferrous oxalate acquired at early (0.5 ps, purple line) and late (2.8 ns, orange line) time points compared to the spectrum obtained from the subtraction of ground-state ferrous and ferric oxalate data (gray line labeled Fe^{2+}–Fe^{3+} oxalate). The initial transient spectra are well-described by a reduction from ferric oxalate to ferrous oxalate based on the correspondence of the gray and purple lines, but agreement in the 1600–1650 region is poorer at the later time point.

The transient IR data show evidence of additional chemical processes after the formation of ferrous oxalate. First, the loss of the ν_{as}(C–O) signal from ferrioxalate showed slower and more complex kinetics, with one fast exponential decay constant of 0.4 ± 0.1 ps and one slow decay constant of 3.8 ± 0.2 ps. As described further below, dissociation of the photo-oxidized oxalate molecule likely occurs on this time scale. Second, the line shape in the 1660–1600 cm^{-1} region evolves and, after 20 ps, is no longer described by a simple model, in which ferrioxalate is reduced to ferrous oxalate. A new absorption feature emerges centered around 1631 cm^{-1} that we tentatively attribute to the solvated CO_2 radical anion.

Mid-IR bands attributed to the ν_3 asymmetric stretch of $CO_2^{\bullet-}$ have been identified at a low temperature in neon at 1658.3 cm^{-1}(28) and argon at 1657.0 cm^{-1} (29) and at room temperature in KBr at 1671 cm^{-1}.(30) Alkali metals spontaneously reduce CO_2, and the IR spectra of complexes such as $Li^+CO_2^{\bullet-}$ appear around 1600 cm^{-1}.(31) However, to the best of our knowledge, no mid-IR spectra of $CO_2^{\bullet-}$ in water or D_2O has been published. We attempted to measure the mid-IR spectra of $CO_2^{\bullet-}$ by generating it through formate photolysis(32) in a flow cell but were unsuccessful.

Therefore, we used *ab initio* simulations to aid in the interpretation of the time-resolved vibrational spectra.

3.2 **Predicted Vibrational Signatures of Candidate Intermediate Species**

We predicted the structure and IR spectra of CO_2, $CO_2^{\bullet -}$, $C_2O_4^{2-}$, and $C_2O_4^{\bullet -}$ using MP2 (Figure 3) and these molecules plus $Fe^{III}(C_2O_4)_3^{3-}$ and $Fe^{II}(C_2O_4)_2^{2-}$ using DFT (Figure S1 of the Supporting Information) and compared the predictions to experimental values for CO_2 (Table S1 of the Supporting Information). The DFT calculations underestimated the C–O bond length and the vibrational frequencies, while MP2 gave better agreement with the experiment. MP2 accuracy tended to increase with increasing basis-set size, although no simulation provided optimal agreement to the positions of the ν_2 and ν_3 stretching bands, and we chose the aug-cc-pvtz basis set for the simulations in this study.

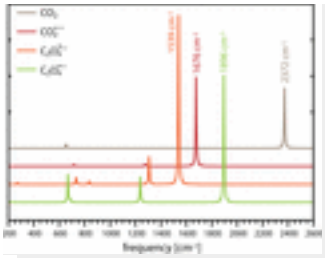

Figure 3. Theoretically predicted IR spectra of CO_2, $CO_2^{\bullet -}$, $C_2O_4^{2-}$, and $C_2O_4^{\bullet -}$ in water simulated using MP2 with the aug-cc-pvtz basis set and an implicit water model.

The excess electron in $CO_2^{\bullet -}$ adds charge density to an antibonding orbital, lengthening the C–O bonds and lowering the symmetry to form a bent triatomic molecule with a OCO angle of ca. 134°. The ν_3 antisymmetric stretch is shifted from 2349 cm^{-1} in CO_2 to a predicted value of 1676.2 cm^{-1}in $CO_2^{\bullet -}$ (Table S2 of the Supporting Information), a value within 40 cm^{-1} of the experimentally observed feature. Because the accuracy of the predicted frequencies with MP2/aug-cc-pvtz is not better than 30 cm^{-1}, the calculation supports our assignment of this new feature. Additional simulations described below suggest that $CO_2^{\bullet -}$ may remain in the iron(II) coordination sphere for many nanoseconds and interactions with the iron(II) complex may influence ligand vibrations.

3.3 **Mid-IR Transient Absorption Spectroscopy in H_2O**

Photoexcitation of ferrioxalate in water generates a new absorption peak at 2339 cm^{-1}, corresponding to the ν_3 asymmetric stretching band for dissolved CO_2(33) that grows in intensity to a maximum and final value at ~40 ps (Figure 4). The data thus show that the $C_2O_4^{\bullet -}$ anion is unstable following ultrafast electron transfer to iron and undergoes dissociation within a sufficiently short period that it cannot play a further role as a reaction intermediate. Molecular simulations, presented

below, predict that the lifetime of the $C_2O_4^{\cdot -}$ anion is short because it has a low energy barrier for dissociation.

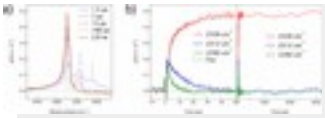

Figure 4. Transient mid-IR data for ferrioxalate in H_2O. (a) Selected transient spectra from 1.5 ps to 2.8 ns. (b) Kinetics extracted at 2339 cm^{-1} (red), 2312 cm^{-1}(blue), and 2290 cm^{-1} (green) shown at short- and long-time scales. Kinetic fits are shown as dashed black lines in the left panel.

Two additional peaks in the transient IR data at 2312 and 2290 cm^{-1} and possibly a third appear within the first picosecond after excitation and are lost within 40 ps, a period in which the CO_2(aq) signal increases to its maximum and final value. The IR data indicate that the CO_2 molecules generated by dissociation of the $C_2O_4^{\cdot -}$ anion are in vibrationally excited states, causing the $\nu_3$vibration frequency to be anharmonically shifted to a higher energy. Buback et al. observed a similar asymmetric broadening of the ν_3 vibrational band of CO_2 generated by the UV photolysis of peroxides in dichloromethane.(34) They used an anharmonic oscillator model of Hamm et al. to simulate the ν_3 vibrational band of hot CO_2 at a number of temperatures,(35) concluding CO_2 to be photogenerated at 1400 and 2700 K for the decompositions of *tert*-butyl benzoyl peroxide and *tert*-butyl benzoyl carbonate, respectively. A comparison between our data and the simulations of Buback et al. indicate the temperature of CO_2 generated by $C_2O_4^{\cdot -}$ dissociation to exceed 1000 K (Figure S2 of the Supporting Information).

To quantify the rate of thermal equilibration of hot CO_2, we used a kinetic model in which ground-state CO_2(aq) and two excited states are generated promptly upon ferrioxalate photoexcitation and the excited-state populations diminish, forming ground-state CO_2(aq) with first-order kinetics. The time dependence of the CO_2(aq) signal is then given by

$$I_{CO_2} = I^0_{CO_2} + I^0_{2290}(1 - e^{t/\tau_{2290}}) + I^0_{2313}(1 - e^{t/\tau_{2312}}) \quad (2)$$

where I_{2290}^0 and τ_{2290} are the initial intensity and decay constant, respectively, at the indicated wavenumber. Agreement with the data was obtained for the fitted values given in Table 1.

Table 1. Optimum Values for the Initial Signal Strength and Exponential Decay Time Constants Obtained from Fitting the Model of Equation 2 to the Kinetic Traces of Figure 4

wavenumber	I^0 (mOD)	τ (ps)
2339	0.13 ± 0.01	n/a
2312	0.21 ± 0.01	3.5 ± 0.2
2290	0.15 ± 0.011	2.9 ± 0.2

3.4 Stability of the $C_2O_4^{\cdot -}$ Anion

We used molecular simulation to test the stability of the $C_2O_4^{\cdot -}$ radical relative to CO_2 and $CO_2^{\cdot -}$. This was accomplished by energy minimizing an electron-deficient oxalate molecule as a function of carbon–carbon separation using MP2 and the implicit water model (Figure 5). Our calculations showed that an unpaired (radical) electron in $C_2O_4^{\cdot -}$ is initially delocalized, forming a metastable molecule with a C–C bond length of ∼2 Å. However, $C_2O_4^{\cdot -}$ is unstable with respect to dissociation products at C–C distances exceeding 2.5 Å. Because zero-point vibration energies exceed the energy barrier and because the critical C–C separation is accessible by molecular vibration, the simulations show that $C_2O_4^{\cdot -}$ will spontaneously decompose.(36) In this process, the radical electron localizes on one fragment of $C_2O_4^{\cdot -}$, forming $CO_2^{\cdot -}$, and the remaining portion transforms into a CO_2 molecule. The simulation predicts an energy gain for dissociation that is likely responsible for generating the CO_2 product in a highly excited vibrational state.

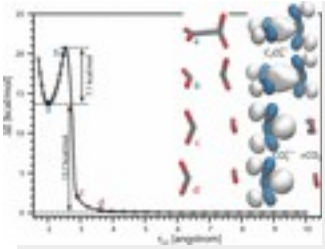

Figure 5. Simulated dissociation of $C_2O_4^{\cdot -}$ into CO_2 and $CO_2^{\cdot -}$. Plotted is the molecular energy as a function of imposed C–C separation (r_{CC}). The geometries and radical e^- orbitals are visualized for a few representative C–C separations: (a) near $C_2O_4^{\cdot -}$ equilibrium (r_{CC} = 2 Å), (b) symmetrically delocalized unpaired electron at

non-equilibrium C–C distance in $C_2O_4^{\cdot -}$ (r_{CC} = 2.5 Å), (c) localized charge/spin on one of the CO_2 part of $C_2O_4^{\cdot -}$ (r_{CC} = 2.9 Å), and (d) CO_2 and $CO_2^{\cdot -}$ products of $C_2O_4^{\cdot -}$ decomposition (r_{CC} = 3.6 Å).

3.5 Loss of CO_2 and $CO_2^{\cdot -}$ from Iron(II)

We developed a molecular dynamics model to simulate the loss of the products of oxalate dissociation from the iron(II) coordination shell. We used 0 K molecular mechanics and conjugate gradient optimization to optimize a starting geometry and, subsequently, ran a series of molecular dynamics simulations in D_2O using the Langevin thermostat. As a result of the stochastic nature of the Langevin thermostat, the system evolution differs among runs, thus allowing for a range of collision-driven diffusion pathways for CO_2 release into solution to be sampled.

In the simulations, CO_2 resided near the Fe^{2+} ion in inner sphere geometry for ~10 ps, jumped to an outer-sphere location for up to ~60 ps, then departed into solution, and exhibited free Fickian diffusion. A total of 3 CO_2 departure pathways of 36 analyzed are shown in Figure 6 (see Movie S1 of the Supporting Information for visualization of the trajectories). The simulations also predict that the $CO_2^{\cdot -}$ anion remains in the iron(II) coordination sphere for at least 100 ps. Although we did not measure or predict the rate of $CO_2^{\cdot -}$ release into solution, this step could contribute to the overall reaction kinetics.

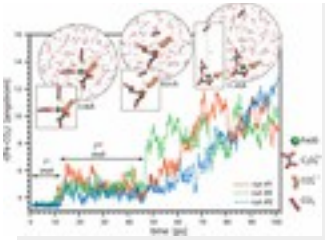

Figure 6. Molecular dynamic simulations of CO_2 leaving the coordination shell of the Fe(II) coordination complex formed by the one-electron oxidation and dissociation of one oxalate molecule in ferrioxalate. A total of 3 CO_2 departure pathways of 36 are shown as plots of the CO_2–Fe distance as a function of time. The $CO_2^{\cdot -}$ radical anion remains bound to iron(II) throughout every simulation up to 10 ns.

3.6 Reaction Mechanism

The time-resolved mid-IR data acquired within 3 ns of photoexcitation, supported by molecular simulations, provide a picture of the initial steps in the pathway of ferrioxalate photolysis (Figure 7). Photon absorption and electron transfer generate an unstable oxalate radical anion, $C_2O_4^{\cdot -}$, that dissociates rapidly, likely on the time scale of a single C–C vibration. Oxalate radical dissociation generates thermally excited CO_2 and $CO_2^{\cdot -}$. The hot CO_2 molecules thermally equilibrate on a time scale of ~40 ps and are predicted to leave the iron(II) coordination sphere within 100 ps. The radical anion, $CO_2^{\cdot -}$, is predicted to remain in the iron(II) coordination sphere for at least 10 ns. The release

and subsequent reactions of $CO_2^{\bullet-}$, including reduction of a further ferrioxalate molecule inferred from the reaction stoichiometry expressed in eq 1, thus occur on a longer time scale than could be probed in this study. This conclusion fits most closely with those of Ogi et al., who observed rapid reduction of iron and proposed the production of CO_2 and the $CO_2^{\bullet-}$ radical.(15) Their detection of ultrafast intramolecular electron transfer, seen in shifts in the Fe K edge, is consistent with our observed ν_{as}(C–O) band shift associated with the transition from ferric to ferrous oxalate.

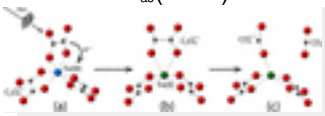

Figure 7. Key species and configurations in the photolysis of ferrioxalate up to 3 ns determined from transient mid-IR data and molecular simulation. (a) One photoexcited oxalate ligand reduces iron(III) within 0.1 ps. (b) Resulting oxalate radical anion, $C_2O_4^{\bullet-}$, dissociates rapidly, likely on the time scale of a single C–C vibration. (c) CO_2 leaves the iron(II) coordination sphere within ∼100 ps, while the radical anion, $CO_2^{\bullet-}$, is predicted to remain in the iron(II) coordination sphere for at least 10 ns.

4 Conclusion

The development of ultrafast laser-based spectroscopies in the mid-IR range in the past decade now allows for organic compound photolysis in aqueous solution to be monitored through the vibrational signatures of reactants, products, and intermediate states. This technique is a powerful probe of environmentally relevant photolysis reactions. It can detect electron transfer and reduction of metal–organic complexes, observe photolysis and the loss of photolysis products from the metal coordination sphere, and capture intermediate species, such as the $CO_2^{\bullet-}$ radical. The experimental results in combination with quantum chemical simulation and classical molecular dynamics reveal molecular steps in the light-driven reaction mechanism of ferrioxalate, clarifying the type and lifetime of intermediates needed to predict the reaction yield as a function of environmental conditions. Such information is critical to correctly model the fluxes of CO_2 to the atmosphere caused by the photolysis of metal-bound organic molecules in sunlit environments and iron–organic photochemistry in aerosols. The time-resolved mid-IR spectroscopy approach used here will find application for the determination of reaction mechanisms and prediction of quantum yields for the large number iron–organic acid complexes that occur in natural ecosystems.

Supporting Information

The Supporting Information is available free of charge on the ACS Publications website at DOI: 10.1021/acsearthspacechem.7b00026.

- Benchmark of theoretical methods for calculating the vibrational frequencies of the CO_2 molecule (Table S1), theoretically predicted vibration frequencies of the $CO_2^{\bullet -}$ radical anion (Table S2), force-field parameters used in molecular dynamics simulations of the Fe–oxalate system (Table S3), theoretically predicted IR spectra of relevant species (Figure S1), experimental TRIR spectrum of CO_2 compared to simulated hot vibrational band absorption (Figure S2), snapshots from molecular dynamics simulations of complexes of iron(III) and iron(II) (Figure S3), and pathways of CO_2 leaving the Fe(II) coordination shell from molecular dynamics simulations (Figure S4) (PDF)

- Visualization of two CO_2 trajectories (Movie S1) (MOV)

- **PDF**
  - sp7b00026_si_001.pdf (1.1 MB)

- **QuickTime Video**
  - sp7b00026_si_002.mov (27.63 MB)

Mechanism of Ferric Oxalate Photolysis

Showing 1/2: sp7b00026_si_002.mov

figshare

1 / 2

Share
Download

The authors declare no competing financial interest.

Acknowledgment

This work was supported by the National Science Foundation under Grant GG-1324791. Benjamin Gilbert was supported by the Chemical Sciences, Geosciences, and Biosciences Division of the

United States Department of Energy (U.S. DOE) under Contract DE-AC02-05CH11231. Use of the Center for Nanoscale Materials, an Office of Science user facility, was supported by the Office of Basic Energy Sciences, Office of Science, U.S. DOE, under Contract DE-AC02-06CH11357.

- Reference QuickView
-

References

This article references 36 other publications.

1. 1.

Weller, C.; Horn, S.; Herrmann, H. Photolysis of Fe(III) carboxylato complexes: Fe(II) quantum yields and reaction mechanisms *J. Photochem. Photobiol., A* **2013**, 268, 24– 36

[Crossref], [CAS]

2. 2.

Sima, J.; Makanova, J. Photochemistry of iron(III) complexes *Coord. Chem. Rev.* **1997**, 160, 161–189

[Crossref], [CAS]

3. 3.

Borer, P.; Hug, S. J. Photo-redox reactions of dicarboxylates and α-hydroxydicarboxylates at the surface of Fe(III) (hydr)oxides followed with *in situ* ATR-FTIR spectroscopy *J. Colloid Interface Sci.* **2014**, 416, 44–53

[Crossref], [PubMed], [CAS]

4. 4.

Faust, B. C.; Zepp, R. G. Photochemistry of aqueous iron(III) polycarboxylate complexes - roles in the chemistry of atmospheric and surface waters *Environ. Sci. Technol.* **1993**, 27 (12) 2517– 2522

[ACS Full Text], [CAS]

5. 5.

Emmenegger, L.; Schonenberger, R. R.; Sigg, L.; Sulzberger, B. Light-induced redox cycling of iron in circumneutral lakes *Limnol. Oceanogr.* **2001**, 46 (1) 49– 61

[Crossref], [CAS]

6. 6.

Cwiertny, D. M.; Young, M. A.; Grassian, V. H. Chemistry and photochemistry of mineral dust aerosol *Annu. Rev. Phys. Chem.* **2008**, 59, 27– 51

[Crossref], [PubMed], [CAS]

7. 7.

Siefert, R. L.; Pehkonen, S. O.; Erel, Y.; Hoffmann, M. R. Iron photochemistry of aqueous suspensions of ambient aerosol with added organic-acids *Geochim. Cosmochim. Acta* **1994**, 58 (15) 3271– 3279

[Crossref], [CAS]

8. 8.

Wu, F.; Deng, N. S. Photochemistry of hydrolytic iron (III) species and photoinduced degradation of organic compounds. A minireview *Chemosphere* **2000**, 41 (8) 1137– 1147

[Crossref], [PubMed], [CAS]

9. 9.

Wu, Y.; Brigante, M.; Dong, W.; de Sainte-Claire, P.; Mailhot, G. Toward a better understanding of Fe(III)-EDDS photochemistry: Theoretical stability calculation and experimental investigation of 4-tert-butylphenol degradation *J. Phys. Chem. A* **2014**, 118 (2) 396– 403

[ACS Full Text], [CAS]

10. 10.

Wang, Z.; Chen, X.; Ji, H.; Ma, W.; Chen, C.; Zhao, J. Photochemical cycling of iron mediated by dicarboxylates: Special effect of malonate *Environ. Sci. Technol.* **2010**, 44 (1) 263– 268

[ACS Full Text], [CAS]

11. 11.

Hatchard, C. G.; Parker, C. A. A new sensitive chemical actinometer. 2. Potassium ferrioxalate as a standard chemical actinometer *Proc. R. Soc. London, Ser. A* **1956**, 235 (1203) 518– 536

[Crossref], [CAS]

12. 12.

Hislop, K. A.; Bolton, J. R. The photochemical generation of hydroxyl radicals in the UV-vis/ferrioxalate/H_2O_2system *Environ. Sci. Technol.* **1999**, 33 (18) 3119– 3126

[ACS Full Text], [CAS]

13. 13.

Chen, J.; Zhang, H.; Tomov, I. V.; Wolfsberg, M.; Ding, X.; Rentzepis, P. M. Transient structures and kinetics of the ferrioxalate redox reaction studied by time-resolved EXAFS, optical spectroscopy, and DFT *J. Phys. Chem. A* **2007**, 111 (38) 9326– 9335

[ACS Full Text], [CAS]

14. 14.

Pozdnyakov, I. P.; Kel, O. V.; Plyusnin, V. F.; Grivin, V. P.; Bazhin, N. M. New insight into photochemistry of ferrioxalate *J. Phys. Chem. A* **2008**, 112 (36) 8316– 8322

[ACS Full Text], [CAS]

15. 15.

Ogi, Y.; Obara, Y.; Katayama, T.; Suzuki, Y. I.; Liu, S. Y.; Bartlett, N. C. M.; Kurahashi, N.; Karashima, S.;Togashi, T.; Inubushi, Y.; Ogawa, K.; Owada, S.; Rubesova, M.; Yabashi, M.; Misawa, K.; Slavicek, P.;Suzuki, T. Ultraviolet photochemical reaction of Fe(III)$(C_2O_4)_3^{3-}$ in aqueous solutions studied by femtosecond time-resolved X-ray absorption spectroscopy using an X-ray free electron laser *Struct. Dyn.***2015**, 2 (3) 034901

[Crossref], [PubMed], [CAS]

16. 16.

Lomont, J. P.; Nguyen, S. C.; Harris, C. B. Ultrafast TRIR and DFT Studies of the Photochemical Dynamics of $Co_4(CO)_{12}$ in solution *Organometallics* **2012**, 31 (10) 4031– 4038

[ACS Full Text], [CAS]

17. 17.

Diroll, B. T.; Guo, P.; Chang, R. P. H.; Schaller, R. D. Large transient optical modulation of epsilon-near-zero colloidal nanocrystals *ACS Nano* **2016**, 10, 10099– 10105

[ACS Full Text], [CAS]

18. 18.

Frisch, M. J.; Trucks, G. W.; Schlegel, H. B.; Scuseria, G. E.; Robb, M. A.; Cheeseman, J. R.; Scalmani, G.;Barone, V.; Mennucci, B.; Petersson, G. A.; Nakatsuji, H.; Caricato, M.; Li, X.; Hratchian, H. P.;Izmaylov, A. F.; Bloino, J.; Zheng, G.; Sonnenberg, J. L.; Hada, M.; Ehara, M.; Toyota, K.; Fukuda, R.;Hasegawa, J.; Ishida, M.; Nakajima, T.; Honda , Y.; Kitao, O.; Nakai, H.; Vreven, T.; Montgomery, J. A., Jr.;Peralta, J. E.; Ogliaro, F.; Bearpark, M.; Heyd, J. J.; Brothers, E.; Kudin, K. N.; Staroverov, V. N.;Kobayashi, R.; Normand, J.; Raghavachari, K.; Rendell, A.; Burant, J. C.; Iyengar, S. S.; Tomasi, J.;Cossi, M.; Rega, N.; Millam, J. M.; Klene, M.; Knox, J. E.; Cross, J. B.; Bakken, V.; Adamo, C.; Jaramillo, J.;Gomperts, R.; Stratmann, R. E.; Yazyev, O.; Austin, A. J.; Cammi, R.; Pomelli, C.; Ochterski, J. W.;Martin, R. L.; Morokuma, K.; Zakrzewski, V.

G.; Voth, G. A.; Salvador, P.; Dannenberg, J. J.; Dapprich, S.;Daniels, A. D.; Farkas, Ö.; Foresman, J. B.; Ortiz, J. V.; Cioslowski, J.; Fox, D. J. Gaussian 09, Revision A.02; Gaussian, Inc.: Wallingford, CT, **2016**.

19. 19.

Kohn, W.; Sham, L. J. Self-consistent equations including exchange and correlation effects *Phys. Rev.* **1965**,140, A1133– A1138

[Crossref]

20. 20.

Møller, C.; Plesset, M. S. Note on an approximation treatment for many-electron systems *Phys. Rev.* **1934**,46, 618– 622

[Crossref], [CAS]

21. 21.

Koch, W.; Holthausen, M. C. A. *A Chemist's Guide to Density Functional Theory*; Wiley: Hoboken, NJ, **2001**.

[Crossref]

22. 22.

Wang, J.; Wolf, R. M.; Caldwell, J. W.; Kollman, P. A.; Case, D. A. Development and testing of a general Amber force field *J. Comput. Chem.* **2004**, 25, 1157– 1174

[Crossref], [PubMed], [CAS]

23. 23.

Li, P.; Merz, K. M., Jr. Taking into account the ion-induced dipole interaction in the nonbonded model of ions*J. Chem. Theory Comput.* **2014**, 10, 289– 297

[ACS Full Text], [CAS]

24. 24.

Li, P.; Song, L. F.; Merz, K. M., Jr. Parameterization of highly charged metal ions using the 12–6-4 LJ-type nonbonded model in explicit water *J. Phys. Chem. B* **2015**, 119, 883– 895

[ACS Full Text], [CAS]

25. 25.

Berendsen, H. J. C.; Grigera, J. R.; Straatsma, T. P. The missing term in effective pair potentials *J. Phys. Chem.* **1987**, 91, 6269– 6271

[ACS Full Text], [CAS]

26. 26.

Case, D. A.; Cerutti, D. S.; Cheatham, T. E., III; Darden, T. A.; Duke, R. E.; Giese, T. J.; Gohlke, H.;Goetz, A. W.; Greene, D.; Homeyer, N.; Izadi, S.; Kovalenko, A.; Lee, T. S.; LeGrand, S.; Li, P.; Lin, C.;Liu, J.; Luchko, T.; Luo, R.; Mermelstein, D.; Merz, K. M.; Monard, G.; Nguyen, H.; Omelyan, I.; Onufriev, A.;Pan, F.; Qi, R.; Roe, D. R.; Roitberg, A.; Sagui, C.; Simmerling, C. L.; Botello-Smith, W. M.; Swails, J.;Walker, R. C.; Wang, J.; Wolf, R. M.; Wu, X.; Xiao, L.; York, D. M.; Kollman, P. A. AMBER 2017; University of California, San Francisco: San Francisco, CA, **2017**.

27. 27.

D'Antonio, M. C.; Wladimirsky, A.; Palacios, D.; Coggiolaa, L.; Gonzalez-Baro, A. C.; Baran, E. J.;Mercader, R. C. Spectroscopic investigations of iron(II) and iron(III) oxalates *J. Braz. Chem. Soc.* **2009**, 20(3) 445– 450

[Crossref], [CAS]

28. 28.

Jacox, M. E.; Milligan, D. E. Vibrational spectrum of CO_2^- in an argon matrix *Chem. Phys. Lett.* **1974**, 28 (2)163– 168

[Crossref], [CAS]

29. 29.

Zhou, M.; Andrews, L. Infrared spectra of the CO_2^{2-} and $C_2O_4^{2-}$ anions isolated in solid argon *J. Chem. Phys.* **1999**, 110, 2414– 2422

[Crossref], [CAS]

30. 30.

Hartman, K. O.; Hisatsune, I. C. Infrared spectrum of carbon dioxide radical anion *J. Chem. Phys.* **1966**, 44(5) 1913– 1918

[Crossref], [CAS]

31. 31.

Kafafi, Z. H.; Hauge, R. H.; Billups, W. E.; Margrave, J. L. Carbon-dioxide activation by lithium metal. 1. Infrared spectra of $Li^+CO_2^-$, $Li^+C_2O_4^-$ and $Li_2^{2+}CO_2^{2-}$ in inert-gas matrices *J. Am. Chem. Soc.* **1983**, 105(12) 3886– 3893

[ACS Full Text], [CAS]

32. 32.

Rosso, J. A.; Bertolotti, S. G.; Braun, A. M.; Mártire, D. O.; Gonzalez, M. C. Reactions of carbon dioxide radical anion with substituted benzenes *J. Phys. Org. Chem.* **2001**, 14 (5) 300– 309

[Crossref], [CAS]

33. 33.

Schaedle, T.; Pejcic, B.; Mizaikoff, B. Monitoring dissolved carbon dioxide and methane in brine environments at high pressure using IR-ATR spectroscopy *Anal. Methods* **2016**, 8 (4) 756– 762

[Crossref], [CAS]

34. 34.

Buback, M.; Kling, M.; Seidel, M. T.; Schott, F. D.; Schroeder, J.; Steegmuller, U. Picosecond IR study of UV-induced peroxide decomposition: Formation and vibrational relaxation of CO_2 in CH_2Cl_2 solution *Z. Phys. Chem.* **2001**, 215, 717– 735

[Crossref], [CAS]

35. 35.

Hamm, P.; Ohline, S. M.; Zinth, W. Vibrational cooling after ultrafast photoisomerization of azobenzene measured by femtosecond infrared spectroscopy *J. Chem. Phys.* **1997**, 106 (2) 519– 529

[Crossref], [CAS]

36. 36.

A total of 3 of 12 vibration modes of $C_2O_4^{\cdot -}$ result in C–C bond stretching. These are infrared-inactive vibrations with theoretically predicted frequencies at 225.2, 694.2, and 1284.7 cm^{-1}. The zero-point vibration energy is equal to 13.97 kcal/mol (with 3.15 kcal/mol coming from the C–C stretching frequencies), which suggests that energy barrier of 7.1 kcal/mol can be overcome by the molecular vibration motion.